

# Disruptive lysosomal-metabolic signaling and neurodevelopmental deficits that precede Purkinje cell loss in a mouse model of Niemann-Pick Type-C disease

**Sarah Kim**

Rowan University

**Kathleen Ochoa**

Rowan University

**Sierra Melli**

Rowan University

**Fawad Yousufzai**

Rowan University

**Barrera Zerian**

Rowan University

**Aela Williams**

Rowan University

**Gianna McIntyre**

Rowan University

**Esteban Delgado**

Rowan University

**James Bolish**

Rowan University

**Vincent Wilson**

Rowan University

**Kelly Maloney**

Rowan University

**Zachary Padron**

Rowan University

**Amaal Khan**

Rowan University

**Rosa Blanco**

University of Puerto Rico, Medical Sciences Campus

**Ileana Soto** (✉ [sotoreyes@rowan.edu](mailto:sotoreyes@rowan.edu))

Rowan University

---

## Article

**Keywords:** NPC1, PTEN, mitochondria, lysosomes, NPC, microglia, mTORC1

**Posted Date:** April 20th, 2022

**DOI:** <https://doi.org/10.21203/rs.3.rs-1559559/v1>

**License:**  This work is licensed under a Creative Commons Attribution 4.0 International License.

[Read Full License](#)

**Additional Declarations:** No competing interests reported.

---

**Version of Record:** A version of this preprint was published at Scientific Reports on April 6th, 2023. See the published version at <https://doi.org/10.1038/s41598-023-32971-0>.

# Abstract

Purkinje cell (PC) loss occurs at an early age in patients and animal models of Niemann-Pick Type C (NPC), a lysosomal storage disease caused by mutations in the *Npc1* or *Npc2* genes. Degeneration of PCs occurs early in NPC, however little is known about how NPC1 deficiency affects the postnatal development of PCs. Using the *Npc1<sup>nmf164</sup>* mouse model, we found that NPC1 deficiency significantly affected the postnatal development of PC dendrites and synapses. The developing dendrites of *Npc1<sup>nmf164</sup>* PCs were significantly deficient in mitochondria and lysosomes. Furthermore, anabolic (mTORC1) and catabolic (TFEB) signaling pathways were not only perturbed but simultaneously activated in NPC1-deficient PCs, suggesting a loss of metabolic balance. We also found that mice with conditional heterozygous deletion of the Phosphatase and Tensin Homolog Deleted on Chromosome 10 gene (*Pten*-cHet), an inhibitor of mTORC1, showed similar early dendritic alterations in PCs to those found in *Npc1*-deficient mice. However, in contrast to *Npc1<sup>nmf164</sup>* mice, *Pten*-cHet mice exhibited the overactivation of the mTORC1 pathway but with a strong inhibition of TFEB signaling, along with no dendritic mitochondrial reductions by the end of their postnatal development. Our data suggest that disruption of the lysosomal-metabolic signaling in PCs causes dendritic and synaptic developmental deficits that precede and promote their early degeneration in NPC.

## Introduction

NPC is an inherited lysosomal storage disease characterized by a neurovisceral accumulation of lipids that leads to neurodegeneration, ataxia, dementia, and death. Although the onset of disease can occur at any age, the classic presentation of NPC is often found between middle to late childhood, when early symptoms such as clumsiness, vertical gaze palsy, gait disturbances, and eventually ataxia are evident<sup>1</sup>. As the disease progresses other neurological symptoms like cognitive impairment, primary behavioral disturbances, severe motor deficits, and dementia take form<sup>2</sup>. Interestingly, cases of adult-onset NPC have been pre-diagnosed with mental disorders such as schizophrenia, attention deficit hyperactivity disorder (ADHD), and depression suggesting that neural circuitry dysfunction precedes the neurological symptoms<sup>2,3</sup>. Importantly, 80–90% of the NPC cases are caused by pathogenic variants in the *Npc1* gene that include small intragenic deletions/insertions, and missense, nonsense, and splice site variants<sup>1</sup>. NPC1 is a lysosomal and endosomal membrane protein that transports cholesterol out of these organelles. PCs are particularly susceptible to NPC1 deficiency by degenerating earlier and to a greater severity than other neurons in the brain<sup>4</sup>. Previous studies have shown significant changes in cerebellar synapses and glial phenotypes along with behavioral and motor deficits during postnatal development and before PC degeneration<sup>5–7</sup>. However, little is known about how *Npc1* deficiency affects PC development. Recent work in our laboratory demonstrated that the postnatal development of cerebellar microglia and the refinement of climbing fiber synapses were significantly altered in NPC1-deficient mice<sup>5</sup>. To expand our understanding of how developmental deficits precede the dysfunction and degeneration of neurons in NPC disease, in this study we investigated how NPC1 deficiency in mice affects the postnatal development of Purkinje cell dendrites.

It is known that mutations in *Npc1* produce the dysfunction of the proteolytic lysosomal pathway in cells<sup>8,9</sup>, which directly affects functions like autophagy<sup>10</sup>. Lysosomal dysfunction in NPC, and in other LSDs<sup>11</sup>, is concomitant with structural abnormalities and ectopic dendrites found in mature neurons from NPC patients and animal models<sup>12,13</sup>, suggesting that lysosomal dysfunction caused by *Npc1* deficiency modifies neuronal structure and function. Recent studies have demonstrated the central role of lysosomes in cellular metabolism<sup>14</sup>. In fact, the lack of lysosomal NPC1 causes the hyperactivation of the mTORC1 pathway, an evolutionarily conserved nutrient sensor that is the center of signaling networks that regulate cellular metabolic processes and growth<sup>15</sup>. Furthermore, it was recently shown that hyperactivation of mTORC1 by NPC1 deficiency triggers lysosomal proteolytic dysfunction and mitochondria damage in different cell culture models including neuronal cultures<sup>8</sup>, suggesting that lack of NPC1 disrupts cellular metabolism.

Since neuronal development is a complex and high-energy process that involves the extension, patterning, and connectivity of neuronal processes<sup>16</sup>, we hypothesized that NPC1 deficiency in mice will lead to pathological changes in the postnatal development of PC dendrites by disrupting lysosomal-metabolic signaling. Given that mutations associated with regulation of the mTORC1 pathway (e.g. *Pten*, *Tsc1*, *Tsc2*, *Pi3k*) lead to neurodevelopmental disorders like autism spectrum disorder<sup>17</sup>, it is imperative to understand the role of regulatory metabolic pathways in neurodevelopment. Therefore, in this study using the *Npc1<sup>nmf164</sup>* mouse, a late-onset mouse model of NPC<sup>18</sup>, we investigated the effects of NPC1 deficiency in the postnatal development of PC dendrites and their metabolic signaling. More particularly, we studied the temporal and spatial activation of proteins associated with anabolic and catabolic pathways that are regulated by the mTORC1 in healthy and *Npc1<sup>nmf164</sup>* PCs. Additionally, we performed similar analyses in mice with heterozygous conditional deletion of the *Pten* gene in PCs; PTEN is an endogenous inhibitor of the mTORC1 pathway<sup>19</sup>. The *Pten-cHet* mice were used to differentiate the pathological changes induced by the disruption of the mTORC1 pathway from the pathology caused by disruption of the same pathway but with lysosomal dysfunction, which is the case of the NPC disease.

## Results

# NPC1 deficiency disrupts postnatal development of Purkinje cell dendrites and synapses

Given that PC dendrites and synapses develop postnatally in mice, we examined how NPC1 deficiency alters PC dendrites at postnatal day 14 (P14) and 30 (P30) in *Npc1<sup>nmf164</sup>* mice using the Golgi-Cox technique. Quantitative analysis of PC dendrites showed a small but significant increase in the dendritic total length in *Npc1<sup>nmf164</sup>* mice when compared to WT mice at P14 (Fig. 1a-b). However, at P30, the dendritic total length was significantly reduced in *Npc1<sup>nmf164</sup>* mice when compared to WT mice (Fig. 1a-b). Although no differences were found between P14 and P30 dendritic length in *Npc1<sup>nmf164</sup>* mice, the dendritic length in WT mice was significantly increased at P30 when compared to P14 mice (Fig. 1b).

Similarly, the Sholl-analysis of PC dendrites indicated that *Npc1<sup>nmf164</sup>* mice had a higher number of branches than WT mice at P14 (Fig. 1c). However, a significant reduction of branches in P30 *Npc1<sup>nmf164</sup>* mice was found when compared to WT mice (Fig. 1d), suggesting that deficiency of NPC1 causes an early and brief overgrowth of dendrites that is not sustained through the last two weeks of postnatal development. These changes in dendritic development were concomitant with similar changes in blood capillaries at the molecular layer (ML), which develop and grow along PC dendrites during postnatal development (Supp Fig. 1). The total length of Lectin immunostained capillaries and terminal points were significantly reduced in *Npc1<sup>nmf164</sup>* mice at P30 when compared to WT mice (Supp Fig. 1).

Since the formation of PC synapses with Parallel fibers occurs along with the growth of dendrites, mice expressing enhanced-GFP in PCs were used to visualize dendrites and spines. WT-*PCP2<sup>EGFP</sup>* and *Npc1<sup>nmf164</sup>-PCP2<sup>EGFP</sup>* mice were generated and immunostained with VGLUT1 to analyze synapses between GFP<sup>+</sup> PC dendritic spines and VGLUT1<sup>+</sup> parallel fibers presynaptic terminals. It is presumed that VGLUT1<sup>(+)</sup>-GFP<sup>+</sup> PC spines are more mature than VGLUT1<sup>(-)</sup>-GFP<sup>+</sup> PC spines because they are establishing synaptic contact with VGLUT1<sup>(+)</sup> presynaptic terminals. At P14 the total number of dendritic spines was significantly higher in *Npc1<sup>nmf164</sup>* mice than in WT mice (Fig. 1e and f). However, the majority of these spines at P14 were not colocalizing with VGLUT1<sup>+</sup> presynaptic terminals (Fig. 1e and g), since the number of VGLUT1<sup>(-)</sup>-GFP<sup>+</sup> PC spines was significantly higher in *Npc1<sup>nmf164</sup>* mice than in WT mice (Fig. 1e and h). A significant reduction in the total number of spines was quantified in P21 *Npc1<sup>nmf164</sup>* mice when compared to P14 *Npc1<sup>nmf164</sup>* and P21 WT mice. While the number of VGLUT1<sup>(+)</sup>-GFP<sup>+</sup> PC spines in P21 *Npc1<sup>nmf164</sup>* mice was significantly decreased when compared to WT mice (Fig. 1g), a significant loss of VGLUT1<sup>(-)</sup>-GFP<sup>+</sup> PC spines was found in P21 *Npc1<sup>nmf164</sup>* when compared to P14 *Npc1<sup>nmf164</sup>* (Fig. 1h), suggesting that immature spines in *Npc1<sup>nmf164</sup>* mice were not able to establish connections with VGLUT1<sup>+</sup> presynaptic terminals.

Given that microglia play important roles in developmental synapse elimination and refinement, their potential involvement in the significant reduction of PC dendrites and spines was investigated in developing *Npc1<sup>nmf164</sup>* mice. The interaction between IBA1<sup>+</sup>/CD68<sup>+</sup> microglia and GFP<sup>+</sup> PC dendrites was analyzed as previously reported<sup>5,7</sup> using the 3D surface rendering tool from Imaris software (see methods) to determine the percentage of GFP<sup>+</sup> dendritic volume contacted or wrapped by microglia in *Npc1<sup>nmf164</sup>* and WT mice. At P21, significantly increased volumes of GFP were found in *Npc1<sup>nmf164</sup>* microglia when compared to microglia from WT mice (Fig. 2a-c), suggesting an increased interaction and engulfment of GFP<sup>+</sup> dendrites by microglia in *Npc1<sup>nmf164</sup>* mice. Additionally, we found that microglia were also engulfing significantly more VGLUT1<sup>+</sup> PF presynaptic terminals in P21 *Npc1<sup>nmf164</sup>* mice than in P21 WT mice (Fig. 2d-e). These data suggest that after the first two weeks of postnatal development, PCs in *Npc1<sup>nmf164</sup>* mice are unable to continue growing and developing functional dendrites and synapses leading to the increased interaction of these structures with microglia.

# NPC1-deficient Purkinje cells have reduced mitochondrial and lysosomal volume in dendrites

Neuronal development is a high-energy demanding process that requires the growth and patterning of complex dendrites and synaptic connections. As it is known, NPC1 deficiency causes lysosomal dysfunction and mitochondrial damage *in vitro*<sup>8,20</sup>. Therefore, we examined the levels of PDE<sup>+</sup> mitochondrial and LAMP1<sup>+</sup> lysosomal volume in PC dendrites at different stages of postnatal development in *Npc1<sup>nmf164</sup>* and WT mice. Using the Imaris 3D surface rendering tool we were able to select and measure the total volume of PDE immunostained mitochondria and LAMP1 immunostained lysosomes in CALB immunostained PCs (Supp Fig. 2). Our data showed that the percent volume of mitochondria in PC dendrites of WT mice slightly decreased between 14 and 30 days after birth, which could be the result of existent mitochondria at P14 becoming sparser throughout larger dendritic trees at P30. However, the percentage of mitochondria volume in PC dendrites from *Npc1<sup>nmf164</sup>* mice was significantly decreased at P14, P21, and P30 when compared to WT mice (Fig. 3a-b and d). However, when compared to WT mice, the percentage of LAMP1 + lysosomal volume in PC dendrites from *Npc1<sup>nmf164</sup>* mice was lesser at P14 and P30, but the same at P21 (Fig. 3a and c). This suggests that at P21 a brief increase of lysosomes occurs in NPC1-deficient PCs.

It has been suggested that lysosomal dysfunction in NPC can lead to the fragmentation and accumulation of damaged mitochondria due to the disruption of catabolic-lysosomal pathways like mitophagy<sup>8</sup>. In fact, here we found that not only the levels of mitochondrial volume in the dendrites of *Npc1<sup>nmf164</sup>* PCs were decreased, but also the PDE<sup>+</sup> mitochondria appeared fragmented in the dendrites of these mice at P30 (Fig. 3d). We examined the levels of mitochondrial and lysosomal volume in *Npc1<sup>nmf164</sup>.Pcp2<sup>EGF</sup>* mice at 12 weeks of age when severe degeneration of PCs occurs<sup>7</sup>, and found that at this stage of neurodegeneration, the percentage of mitochondrial and lysosomal volume in PC dendrites from *Npc1<sup>nmf164</sup>* mice was significantly reduced when compared to WT mice (Fig. 4a-d). Additionally, mitochondria in *Npc1<sup>nmf164</sup>* dendrites were not only fragmented but also aggregated in swollen dendritic portions of NPC1-deficient PC dendrites (Fig. 4b). These findings were also confirmed using transmission electron microscopy, where healthy elongated mitochondria were observed in PC dendrites from 12wks WT mice, while fragmented, rounded, and aggregated mitochondria were observed in swollen degenerating dendrites from 12wks *Npc1<sup>nmf164</sup>* mice (Fig. 4e-f). These results support the hypothesis that impaired lysosomal function in NPC leads to the aggregation of damaged mitochondria which can lead to metabolic deficits and cell death. Our data also demonstrated that this pathological accumulation of damaged mitochondria in PC dendrites occurs early during development preceding and persisting through the degeneration of PCs in NPC.

## Disruptive lysosomal-metabolic signaling in developmental *Npc1<sup>nmf164</sup>* Purkinje cells

It is well known that lysosomal cholesterol accumulation caused by NPC1 deficiency in different *in vitro* cell culture models leads to the hyperactivation of the anabolic mTORC1 pathway<sup>8,20</sup>. It was intriguing to

find that the size of the PC dendritic trees and the number of spines were increased in P14 *Npc1<sup>nmf164</sup>* mice when compared to WT mice. We hypothesized that this increase was the result of mTORC1 hyperactivation. To test this, we used an antibody against a specific downstream target of the mTORC1 pathway, the phosphorylated S6 ribosomal (pS6R) protein. Strong immunolabeling of pS6R was observed in somas of PCs from *Npc1<sup>nmf164</sup>* and WT mice (Fig. 5a). However, pS6R immunostaining was significantly higher in PC dendrites from P14 *Npc1<sup>nmf164</sup>* mice when compared to P14 WT mice (Fig. 5a-b). Also, P14 WT mice showed higher levels of dendritic pS6R immunostaining when compared to P21 WT mice. These data suggest that activation of mTORC1 occurs in dendrites during stages of active growth (P14), but NPC1 deficiency induces a further increase of this basal activation that could be causing the increased growth of dendrites in P14 *Npc1<sup>nmf164</sup>* mice.

Since the mTORC1 pathway is associated with the activation of anabolic pathways such as lipid biogenesis<sup>21</sup>, we investigated the levels of the fatty acid synthase (FASN) protein in PCs using immunofluorescence. Transcription of FASN is regulated by the sterol regulatory element binding protein 1 (SREBP1) transcription factor<sup>22,23</sup>, which can be activated by the mTORC1 signaling<sup>21,24,25</sup>. Quantitative analysis of FASN fluorescence intensity in PC bodies showed that FASN levels were higher in P14 WT mice when compared to P21 WT mice (Fig. 5c-d). PCs from P14 *Npc1<sup>nmf164</sup>* mice showed higher levels of FASN when compared to PCs from P14 WT and P21 *Npc1<sup>nmf164</sup>* mice (Fig. 5c-d). This suggests that, like mTORC1, FASN levels are increased in PCs during stages of dendritic growth and that hyperactivation of mTORC1 in *Npc1<sup>nmf164</sup>* PCs may be leading to the heightened increase of FASN in these mice.

Finally, because activation of the mTORC1 pathway leads to the blockage of the transcription factor EB (TFEB), which upon activation induces biogenesis of lysosomes and activation of catabolic pathways<sup>26,27</sup>, we examined the activation of TFEB in PCs using immunofluorescence. The percentage of PCs with nuclear localization of TFEB, a well-established hallmark of TFEB activation<sup>28</sup>, was determined in WT and *Npc1<sup>nmf164</sup>* mice at postnatal stages. Our data showed that the percentage of nuclear TFEB in PCs while low at P14 in WT PCs was significantly increased by P21 (Fig. 5e-f). However, in *Npc1<sup>nmf164</sup>* mice, the levels of nuclear TFEB were significantly higher at P14 when compared to P14 WT mice, and even higher than P21 WT at P21. It was surprising to find increased levels of TFEB in P14 *Npc1<sup>nmf164</sup>* PCs because the mTORC1 pathway was hyperactivated at this stage. However, it is possible that the decreased levels and dysfunction of lysosomes in NPC1-deficient PCs led to the activation of other upstream pathways that can activate TFEB to compensate for the deficiency. To test this, we proceeded to analyze PCs from PTEN conditional heterozygous (*Pten*-cHet) mice where the mTORC1 pathway can be hyperactivated specifically in PCs that have healthy lysosomes.

### **Pten conditional heterozygosity in Purkinje cells alters their dendritic development**

Previous studies have shown that PC conditional deletion of PTEN leads to cell hypertrophy, age-dependent degeneration, and behavioral deficits<sup>29</sup>. Interestingly, *Pten* heterozygous mutations in humans

and animal models are associated with autism spectrum disorder, macrocephaly, and neuronal hypertrophy including PCs<sup>30,31</sup>. To test if PTEN haploinsufficiency alters PC dendritic development, conditional heterozygous mice for the *Pten* gene (*Pten*-cHet) in PCs were used to examine changes in dendritic development at postnatal ages P14 and P30. Using the Golgi-Cox technique, we found that the dendritic total length and branching in *Pten*-cHet mice were significantly increased at P14 when compared to P14 WT mice but similar to the dendritic total length of P30 *Pten*-cHet and WT mice (Fig. 6a-c). At P30 however, there was no difference in the total length and size of dendritic trees between *Pten*-cHet and WT mice (Fig. 6a-b and d), suggesting that *Pten* haploinsufficiency produces dendritic overgrowth only during the first two weeks of postnatal development.

### **Hyperactivation of the AKT-mTORC1 pathway in *Pten* conditional heterozygous Purkinje cells**

PTEN is a well-known inhibitor of the AKT-mTORC1 pathway<sup>19</sup>. To determine if *Pten* haploinsufficiency in PCs induces the hyperactivation of AKT, PCs immunostained with phosphorylated AKT (pAKT) and CALB were analyzed at P14 in *Pten*-cHet and WT mice. We found that immunostaining of pAKT was significantly higher in PCs from *Pten*-cHet at P14 when compared to WT mice (Fig. 7a and d), confirming that *Pten* haploinsufficiency causes the hyperactivation of AKT in PCs. To determine if the overactivation of AKT in *Pten*-cHet PCs leads to the increased activation of mTORC1 pathway, pS6R immunoreactivity was analyzed in P14 *Pten*-cHet PCs. We found that the pS6R volume in CALB<sup>+</sup> PCs was significantly greater in dendrites from *Pten*-cHet mice when compared to WT mice (Fig. 7b and e). Similarly, the immunoreactivity of the mTORC1 downstream protein FASN was found to be significantly higher in *Pten*-cHet mice than in WT mice (Fig. 7c and f), suggesting that haploinsufficiency of *Pten* in P14 mice leads to the hyperactivation of the AKT-mTORC1 pathway, increased lipid biogenesis, and overgrowth of PC dendrites in these mice. Importantly, as expected nuclear translocation of TFEB, which is inhibited by both AKT and mTORC1 pathways, was significantly lower (almost none) in *Pten*-cHet PCs when compared to WT mice (Fig. 7g).

Contrary to *Npc1<sup>nmf164</sup>* mice, *Pten*-cHet mice should have healthy and functional lysosomes. However, it is expected that due to the hyperactivation of the AKT-mTORC1 pathway and the lack of activation of TFEB, the biogenesis of lysosomes may be decreased in the PCs of these mice. After examining P14 and P30 *Pten*-cHet mice we found that the percentage of LAMP1<sup>+</sup> lysosomal volume in CALB<sup>+</sup> PC dendrites was significantly decreased in P14 *Pten*-cHet mice when compared to WT mice (Fig. 8a-b). To determine if overactivation of the AKT-mTORC1 pathway in *Pten*-cHet mice led to changes in mitochondrial volume levels in dendrites, the percentage of PDE<sup>+</sup> mitochondrial volume was measured in CALB<sup>+</sup> PCs. Our results showed that the percentage of mitochondrial volume in PC dendrites at P14 was significantly decreased in *Pten*-cHet mice when compared to WT mice (Fig. 8a and c). Conversely, at P30 the percentage of mitochondria volume in PC dendrites was significantly increased in *Pten*-cHet mice when compared to WT mice (Fig. 8a and c). These results suggest that mitochondria biogenesis in *Pten*-cHet may increase after the first two weeks of postnatal development to compensate for the early overgrowth of dendrites even when no further overgrowth of dendrites occurred after the first two postnatal weeks.

Overall, these findings have shown that early dendritic overgrowth and overactivation of the mTORC1 pathway (pS6R) in PCs occur in both *Npc1<sup>nmf164</sup>* and *Pten-cHet* mouse strains (Fig. 8d). However, simultaneous and persistent overactivation of TFEB and decreased levels of mitochondrial volume were only found in *Npc1<sup>nmf164</sup>* PCs where significant dendritic atrophy by the end of postnatal development occurs (Fig. 8d), suggesting that disruptive lysosomal-metabolic signaling and -dysfunction are the culprit of neurodevelopmental defects in NPC1 deficient PCs.

## Discussion

Given that NPC patients are still developing their brains at the time of disease onset, we were intrigued by how lack of NPC1 impacts neurodevelopment and predisposes neurons to early degeneration. Importantly, the development of early neurological symptoms such as clumsiness, gait defects, and ataxia in both the human disease and animal models are a direct consequence of early dysfunction and degeneration of cerebellar PCs. However, little is known about how NPC1 deficiency affects PCs development and if neurodevelopmental deficits precede their precipitated death. Given the abrupt early loss of PCs in NPC during childhood and juvenile ages, we hypothesized that in the *Npc1<sup>nmf164</sup>* mouse postnatal development, alterations of PCs precede and predispose these neurons to cell death. Previous studies in our laboratory showed pathological changes in the postnatal development of cerebellar microglia in *Npc1<sup>nmf164</sup>* mice, including increased engulfment of PC dendrites and phagocytic activity at P30<sup>7</sup>. Based on these results, we were curious about how NPC1 deficiency was specifically affecting the development of PC dendrites and synapses. The results of our study showed that not only NPC1 deficiency impacts the development and metabolic signaling of PC dendrites, but also has contrasting effects through different stages of postnatal development. For instance, a small but significant increase in the size of PC dendritic trees in P14 *Npc1<sup>nmf164</sup>* mice was concomitant with the increased levels of pS6R and FASN, both downstream products of mTORC1 activation. Hyperactivation of the mTORC1 pathway due to NPC1 deficiency has been demonstrated in several cell culture models including iPSC-derived neurons<sup>8,32</sup>. Similarly, higher levels of pS6R and FASN were found in PCs from *Pten-cHet* mice, where a major overgrowth of PC dendrites was also found at P14. Increased levels of the FASN protein are a hallmark of increased activation of the SREBP1 transcription factor, which regulates the expression of genes that control lipid biogenesis and homeostasis<sup>33</sup>. Regulation of the SREBP transcription factors by the mTORC1 pathway contributes to cell growth<sup>21,24,25</sup>. SREBPs and the activation of fatty acid synthesis play important roles in the dendritic development of neurons of *Drosophila* larvae<sup>34,35</sup> and mouse hippocampal neurons<sup>36</sup>. Our results suggest that hyperactivation of mTORC1 in PCs leads to the increased activation of anabolic pathways as demonstrated by the increased phosphorylation of S6R and synthesis of the FASN protein in P14 *Npc1<sup>nmf164</sup>* and *Pten-cHet* PCs. Further studies are necessary to confirm if the overactivation of SREBP1 transcription factor in PCs from these mice is directly caused by the hyperactivation of the mTORC1 pathway.

Structural abnormalities and ectopic dendrites have been found in neurons from NPC patients, as well as mouse and cat animal models<sup>12,13</sup>, suggesting that lysosomal dysfunction impacts neuronal structure and function. Our results are in line with these findings as deficiency of NPC1 yielded significant changes in the development of PC dendrites and synaptic structures. In fact, the overgrowth of dendrites and spines found in *Npc1<sup>nmf164</sup>* PCs at P14 was not sustained through the third and fourth week of postnatal development. Moreover, the dendritic trees of *Npc1<sup>nmf164</sup>* PCs were significantly reduced at P30 when compared to WT mice. These results coincided with the lack of hyperactivation of the S6R protein and the stabilization of the FASN protein levels at P21 in *Npc1<sup>nmf164</sup>* PCs, both proteins levels were similar to WT. Overactivation of anabolic processes during growth could lead to states of nutrient starvation and low energy, leading to inhibition of mTORC1<sup>37</sup>. However, while the levels of these mTORC1 downstream proteins were similar between *Npc1<sup>nmf164</sup>* and WT mice at P21, at P30 the size of the PC dendritic trees in *Npc1<sup>nmf164</sup>* were still significantly smaller than the WT PC dendritic trees. Furthermore, in *Pten*-cHet PCs where the mTORC1 pathway was also overactivated at P14, the PC dendritic trees were not reduced but were instead similar to WT cells in P30 mice. These results suggested that other pathological changes associated with lysosomal dysfunction in *Npc1<sup>nmf164</sup>* mice were driving the dendritic atrophy at P30. Given that mTORC1 activation leads to the inhibition of TFEB nuclear translocation and activation, we were expecting to find decreased nuclear translocation of TFEB in *Npc1<sup>nmf164</sup>* mice at P14. However, nuclear translocation of TFEB in PCs was significantly increased in these mice at P14 and P21. Interestingly, at P21 decreased pS6R levels coincided with increased nuclear translocation of TFEB in WT PCs, suggesting that activation of catabolic pathways at this age may be associated with the process of dendritic remodeling (from multiplanar to monoplanar) that occurs in these cells between P18 and P25<sup>38</sup>. As anticipated, and contrary to the findings in *Npc1<sup>nmf164</sup>* mice, *Pten*-cHet PCs exhibited a significant decrease in TFEB nuclear translocation when compared to WT mice. *Pten* haploinsufficiency is expected to induce the overactivation of the AKT-mTORC1 pathway; both AKT<sup>39,40</sup> and mTORC1<sup>41,42</sup> can inhibit TFEB nuclear translocation leading to the inhibition of catabolic pathways. It is possible that lysosomal dysfunction in NPC not only causes the aberrant overactivation of the mTORC1 pathway, but also the co-activation of other molecular pathways that respond to lysosomal deficits. One possible mechanism driven by lysosomal dysfunction to co-activate TFEB in *Npc1<sup>nmf164</sup>* mice is the deregulation of intracellular Ca<sup>2+</sup>. NPC1-deficient cells have decreased levels of lysosomal and endoplasmic reticulum (ER) -luminal Ca<sup>2+</sup> and increased influx of Ca<sup>2+</sup> at the plasma membrane resulting in an increased resting cytosolic Ca<sup>2+</sup><sup>43-45</sup>. This increased intracellular Ca<sup>2+</sup> can activate cytoplasmic calcineurin, a phosphatase that induces TFEB nuclear translocation after dephosphorylating it<sup>46-48</sup>, suggesting that the aberrant activation of TFEB in *Npc1<sup>nmf164</sup>* PCs may be the consequence of the deregulation of the Ca<sup>2+</sup> signaling. Future studies are needed to determine if Ca<sup>2+</sup> deregulation in NPC leads to the aberrant activation of TFEB in developing PCs.

Another potential trigger of TFEB activation is the accumulation of damaged mitochondria<sup>49</sup>. The biogenesis of mitochondria is significantly decreased in NPC1-deficient cells due to lysosomal

dysfunction<sup>50</sup>, and the accumulation of damaged mitochondria in these cells is a direct consequence of mTORC1 hyperactivation<sup>8</sup>. Our results suggest that in *Npc1<sup>nmf164</sup>* mice, the significant deficiency of healthy mitochondria and the accumulation of the damaged type could also be triggers of TFEB overactivation. First, we found that the levels of PDE<sup>+</sup> mitochondria in PC dendrites were significantly reduced through all the analyzed postnatal stages, supporting the idea that PC mitochondria deficits are an early event that precedes neurodegeneration in NPC. Then, accumulation of damaged mitochondria in atrophied dendrites from degenerating PCs was found in 12wks *Npc1<sup>nmf164</sup>* mice. Given that lysosomes and mitochondria are important mediators of cellular metabolism, it is expected that they play key roles in neuronal development, which is not only complex but also a high energy process that includes the extension, patterning, and connectivity of neuronal processes<sup>16</sup>. Increased trafficking of lysosomes to dendrites and spines during development and in response to synaptic activity has been reported before<sup>51,52</sup>, supporting that lysosomal activity plays a role in dendritic differentiation. In this study, we found that during healthy conditions (WT) the volume of LAMP1<sup>+</sup> lysosomes in developing dendrites was higher at the early stages of development and decreased as they reached maturity. In *Npc1<sup>nmf164</sup>* PCs, the levels of dendritic LAMP1<sup>+</sup> lysosomes were lower than WT at P14 and P30, but increased to WT levels at P21 suggesting that the aberrant activation of TFEB in these mice was driving the short-term increase of dendritic LAMP1<sup>+</sup> lysosomes in NPC. Although the levels of LAMP1<sup>+</sup> lysosomes and PDE<sup>+</sup> mitochondria in *Pten*-cHet PC dendrites were significantly reduced at P14, the levels of dendritic mitochondria at P30 were remarkably higher than in WT PC dendrites. It is likely that after the fast overgrowth of dendrites at P14 in *Pten*-cHet PCs, the biogenesis of mitochondria was activated by energy (ATP) depletion<sup>53</sup> and/or decreased mitophagy activity due to the lack of PTEN<sup>54</sup>. However, contrary to *Npc1<sup>nmf164</sup>* mice, not only were *Pten*-cHet mice able to increase the levels of mitochondria in PC dendrites with maturity, but they were also able to prevent atrophy of the dendritic trees. Additionally, contrary to *Npc1<sup>nmf164</sup>* mice, *Pten*-cHet mice exhibited significant inhibition of TFEB catabolic signaling in PCs, suggesting that lack of catabolic signaling prevents the regression of PC dendritic trees. These results indicate that developing PC dendrites in *Npc1<sup>nmf164</sup>* mice are suffering from noteworthy metabolic deficits that lead to the aberrant and simultaneous overactivation of anabolic and catabolic pathways. This metabolic imbalance is associated with the atrophy of dendrites and the reduction of synaptic contacts at the end of postnatal development. Furthermore, the increased engulfment of these structures by microglia suggests that metabolic deficits in these synaptic structures lead to their inability to establish functional synapses with parallel fibers, making these weak/non-functional synapses a target for pruning by microglia. Engulfment of synaptic inputs during developmental synapse elimination in healthy mice is driven by the lack of synaptic activity, where the weaker synapses are preferentially engulfed by microglia<sup>55</sup>. Overall, this study is showing for the first time that NPC1-deficient mice have remarkable lysosomal-metabolic signaling deficits in PCs during the postnatal development of their dendritic trees that precede and predispose these cells to early degeneration in NPC. In conclusion, our studies highlight the importance of elucidating the role of metabolic balance in the differentiation, expansion, and patterning of neuronal dendrites and how disruption of these pathways leads to neuronal dysfunction and degeneration.

# Methods

## Animals

All experiments involving mice were conducted in accordance with policies and procedures described in the Guide for the Care and Use of Laboratory Animals of the National Institutes of Health and were approved by the Animal Care and Use Committees at the Rowan University School of Osteopathic Medicine. The results and experiments of this study that involves animals are also reported in accordance with ARRIVE guidelines. The C57BL/6J-*Npc1*<sup>nmf164</sup>/J mouse strain (Jax stock number 004817) was provided by Dr. Robert Burgess at The Jackson Laboratory. *Npc1*<sup>nmf164</sup> heterozygous mice were bred and housed in a 12/12-hour light/dark cycle to generate both WT and *Npc1*<sup>nmf164</sup> homozygous mutant mice. To produce NPC1-deficient mice with PCs expressing GFP (*Npc1*<sup>nmf164</sup>-*Pcp2*<sup>EGF</sup>), *Npc1*<sup>nmf164</sup> heterozygous mice were intercrossed with the B6;FVB-Tg(*Pcp2*-EGFP)2Y<sub>uza</sub>/J (Jax stock number 004690). To study changes in mouse PCs dendrites during postnatal development caused by haploinsufficiency of *Pten*, the *Pten*<sup>fl<sup>ox</sup></sup> mouse strain (B6.129S4-*Pten*<sup>tm1Hwu</sup>/J, Jackson stock number 006440) was crossed to the *Pcp2*-*cre* strain (B6.129-Tg(*Pcp2*-*cre*)2Mpin/J, Jackson stock number 004146) to generate F1 heterozygous mice for both *Pten*<sup>fl<sup>ox</sup>/-</sup>/*Pcp2*-*Cre*<sup>+/-</sup> (here will be referred as *Pten*-cHet). Both males and females were used in this study, at a ratio of 2:2 when 4 mice were used. The tissue and results from WT mice used for the NPC1 deficiency studies were also used as a control for the experiments with *Pten*-cHet mice.

## Golgi-Cox staining technique

The Golgi-Cox staining technique was performed using and following the instructions of a commercially available kit (FD Rapid GolgiStain™ Kit, FD NeuroTechnologies Inc.) Briefly, after mice were euthanized with CO<sub>2</sub>, brains were dissected, immersed, and incubated in the impregnating solution (mixed solution A and B) for two weeks. After the two weeks of incubation, the impregnated solution was replaced by the 30% sucrose solution (solution C) and incubated for 72hrs. Then, brains were removed from the solution, quick-froze, and stored at -80° C. For tissue sectioning, the brain was immersed and frozen in optimal compound temperature (OCT) media. Cryostat sections of 160 μm were collected in solution C, then rinsed in distilled water prior to being immersed in the developing solution (solutions D and E). After rinsing the tissue slices in distilled water, they were mounted onto slides, dried, and dehydrated using 75%, 85%, and 100% ethanol prior to being immersed in Histo-Clear II (National Diagnostics). Slides were mounted using Permount and allowed to dry overnight prior to analysis.

## Mouse Perfusion and Tissue Preparation

After mice were euthanized with CO<sub>2</sub>, transcardial perfusion with 1X PBS followed by 4% paraformaldehyde was performed. Brains were carefully dissected and fixed by immersion in 4% paraformaldehyde overnight. After fixation, brains were rinsed in 1X PBS, immersed in 30% sucrose/PBS solution overnight at 4°C, frozen in OCT, and cryosectioned as 40μm and 50μm floating sections.

## Immunohistochemistry

For immunostaining experiments, 40-50 $\mu$ m floating sections were collected in 1X PBS, then rinsed once in 1X PBT (PBS + 1% Triton 100X), and incubated overnight at 4°C in a cocktail of primary antibodies that were diluted in 1X PBT + 20% normal donkey serum. After the overnight incubation, sections were rinsed three times with 1X PBT for 10 min and incubated for 1.5 hours in the corresponding secondary antibodies (1:500, Jackson-ImmunoResearch or Invitrogen). Cerebellar sections were then washed three times with 1X PBT for 10–15 min, incubated with DAPI, and mounted in Poly-aquamount (Polysciences). The following primary antibodies were used: rabbit anti-IBA1 (1:200, Wako, # 019-19741), mouse anti-CALB (calbindin, 1:200, Sigma-Aldrich, #C9848), rat anti-CD68 (1:200, Bio-Rad, #MCA1957), Lycopersicon esculentum(Tomato)-Lectin (1:200, Sigma-Aldrich, #L0401), guinea-pig anti-VGLUT1 (1:800, Synaptic Systems, #135404), rabbit anti-phosphorylated S6R (1:200, Cell Signaling, #2211), rabbit anti-phosphorylated AKT (1:200, Cell Signaling, #8112), rabbit anti-TFEB (1:200, Bethyl Laboratories, A303-673A), rabbit anti-FASN (1:200, Cell Signaling, #3180), rabbit anti-pyruvate dehydrogenase E 1 alpha (1:200, GeneTex, # GTX104015 ), rat anti-CD107a (LAMP-1) (1:200, BioLegend, # 121602).

## Microscopy image analysis

For all the image analyses described below, investigators were blind to the genotype of the mice. PCs stained by the Golgi-Cox technique were imaged with the Keyence BZ-X800 imaging system using the 40X objective and the Quick Full Focus tool. To measure the total length and perform the Sholl-Analysis of these Golgi-Cox-stained PCs, the Simple Neurite Tracer plugin from the ImageJ software was used.

For the quantification of GFP<sup>+</sup> spines that were colocalizing or not with VGLUT1<sup>+</sup> presynaptic inputs from parallel fibers, a Nikon A1R Confocal System equipped with Live Cell 6 Laser Line and Resonant Dual Scanner was used to take 0.8mm images with a 63X objective. To increase the visual magnification of these structures and facilitate the manual quantification of them, high magnified snapshots of the confocal images were taken using the Bitplane Imaris<sup>®</sup> software (Oxford Instruments). Then, these snapshots with scale bars (see images in Figure 1e) were used to measure the length of dendritic processes and manually count (Cell counter plugin) the number of spines per mm using the ImageJ software. Two to three images were taken per mouse (n=4 mice).

For 3D image reconstructions and analyses, three sagittal 50 $\mu$ m cerebellar sections were immunostained by free-floating immunohistochemistry. All the images analyzed by the Bitplane Imaris<sup>®</sup> software were acquired using the Nikon A1R Confocal System. Confocal image stacks were acquired using a 40X objective lens with a 1 $\mu$ m interval through a 40 $\mu$ m z-depth of the tissue. Two to three confocal images per mouse were taken in the cerebellar cortex from the first 4 lobes (anterior region of the cerebellum). To quantify the total length and terminal points of cerebellar capillaries in the cerebellar cortex of postnatally developing mice, the Filament Tracer plugin from the Imaris<sup>®</sup> software was used. Two to three images per mouse (n=4 mice) were used for the quantifications. Quantitative analysis of 3D images to determine the volume of GFP or VGLUT1 inside microglia was performed using the Imaris<sup>®</sup> Surface rendering tool.

First, IBA1<sup>+</sup> microglia were segregated using the Surface rendering tool. Then to quantify GFP from PC dendrites or VGLUT1 synaptic terminals contacted or engulfed by microglia, the “Mask all” tool was used to create a new channel of the GFP<sup>+</sup> or VGLUT1<sup>+</sup> areas inside of the created surface (in this case IBA1 surface) by clearing all the fluorescence that was not found overlapping/contacting the IBA1 rendering surface. The sum of the GFP or VGLUT1 volume contacted or inside the IBA1 surface was calculated and provided by the software then used for the data analysis presented here.

Quantifications of the PDE and LAMP1 total volume inside CALB<sup>+</sup> dendrites were performed by cropping a region in the ML (300µm height X 400µm wide) in 40X confocal images and creating a 3D surface rendering for CALB that was used to obtain the sum of the volume of the CALB<sup>+</sup> dendrites. Then, the “Mask all” tool was used to create a new channel for the PDE<sup>+</sup> or LAMP1<sup>+</sup> areas inside of the created surface (in this case CALB surface) by clearing all the fluorescence that is not found overlapping/contacting the rendering surface. 3D surface renderings were created for the newly created PDE and LAMP1 channels in order to determine the volume of this staining that was inside the CALB<sup>+</sup> dendrites. The Imaris<sup>®</sup> software calculated and provided the measurements of the respective volumes for PDE and LAMP1, and the percentage of these markers in PC dendrites were calculated by dividing them by the CALB volume of the dendrites.

The Imaris<sup>®</sup> surface rendering tool was also used to measure the levels of pS6R and pAKT volume in PC dendrites and soma respectively. FASN fluorescence raw intensity per PC soma was measured using ImageJ, where the soma of the cells was manually traced to select the region of interest for the measurement. The intensity value was then divided by the area of the traced cell. PCs with nuclear labeling of TFEB were manually counted after selecting a region of interest using a box of 50 X 40 pixels and divided by the total number of PCs inside the box to calculate the percentage of PCs with TFEB nuclear labeling. NeuroTrace was used to label the PC soma when FASN and TFEB antibodies were used.

## Electron microscopy

For electron microscopy, WT and *Npc1<sup>nmf164</sup>* mice (12 weeks of age) were perfused with 4% PFA, then brains were dissected and hemisected in the midsagittal plane. One of the hemisections was fixed overnight (2% paraformaldehyde + 2% glutaraldehyde diluted in 0.1 M cacodylate buffer with 0.05% CaCl<sub>2</sub>) for electron microscopy. The process of resin embedding was performed as previously described<sup>7,56</sup>. Briefly, small pieces of the processed cerebella were infiltrated with 50/50 Epon-Araldite resin and propylene oxide for 1 h, then in 100% Epon-Araldite and left in the desiccator overnight. The next day the cerebellum samples were placed in cubic molds and embedded in 100% resin. The resin block was trimmed and, using an ultramicrotome (Sorvall MT-2), longitudinal sections were cut; semi-thin sections (1µm thick) for light microscopy, and ultrathin (90 nm) for electron microscopy. For light microscopy, semi-thin sections were stained using methylene blue-azure II and basic fuchsin. Thin sections were examined with a JEOL JEM-1011 electron microscope equipped with a Gatan digital camera (Model-832) to describe the ultrastructural features of the cerebellar ML.

## Statistical Analysis

Data were analyzed using GraphPad Prism software. Significance was calculated using unpaired t-tests for comparisons between two groups. p-values are provided as stated by GraphPad Prism software and significance was determined with p-values less than 0.05.

## Declarations

### COMPETING INTERESTS

The authors declare that the research was conducted in the absence of any commercial or financial relationships that could be construed as a potential conflict of interest.

### ACKNOWLEDGEMENTS

The authors thank Clarissa del Cueto (RIP) from the Institute of Neurobiology for technical assistance with the EM. To the Department of Biomedical Engineering at Rowan for the use of the confocal microscope. This work was funded in part by NS104994 (IS) and NSF-IOS1941296 (IS), GM116692 and NSF-DBI-0959225 (REB).

### AUTHOR CONTRIBUTIONS

S.K., K.O., F.A.K.Y., S.E.M., Z.D.B., A.A.W., G.M., E.D., J.N.B., V.B.W, K.M., Z.M.P., and A.H.K. performed experiments, R.E.B. performed TEM studies, and I.S. designed all the experiments, oversaw data generation and analysis, and wrote the manuscript. All authors reviewed and approved the final version.

## References

1. Patterson, M. in *GeneReviews(R)* (eds R. A. Pagon *et al.*) (1993).
2. Mengel, E. *et al.* Niemann-Pick disease type C symptomatology: an expert-based clinical description. *Orphanet J Rare Dis* **8**, 166, doi:10.1186/1750-1172-8-166 (2013).
3. Jahnova, H. *et al.* Observational, retrospective study of a large cohort of patients with Niemann-Pick disease type C in the Czech Republic: a surprisingly stable diagnostic rate spanning almost 40 years. *Orphanet J Rare Dis* **9**, 140, doi:10.1186/s13023-014-0140-6 (2014).
4. Vanier, M. T. & Millat, G. Niemann-Pick disease type C. *Clin Genet* **64**, 269–281 (2003).
5. Boyle, B. R. *et al.* NPC1 deficiency impairs cerebellar postnatal development of microglia and climbing fiber refinement in a mouse model of Niemann-Pick disease type C. *Development* **147**, doi:10.1242/dev.189019 (2020).
6. Caporali, P. *et al.* Developmental delay in motor skill acquisition in Niemann-Pick C1 mice reveals abnormal cerebellar morphogenesis. *Acta Neuropathol Commun* **4**, 94, doi:10.1186/s40478-016-0370-z (2016).

7. Kavetsky, L. *et al.* Increased interactions and engulfment of dendrites by microglia precede Purkinje cell degeneration in a mouse model of Niemann Pick Type-C. *Sci Rep* **9**, 14722, doi:10.1038/s41598-019-51246-1 (2019).
8. Davis, O. B. *et al.* NPC1-mTORC1 Signaling Couples Cholesterol Sensing to Organelle Homeostasis and Is a Targetable Pathway in Niemann-Pick Type C. *Dev Cell* **56**, 260–276 e267, doi:10.1016/j.devcel.2020.11.016 (2021).
9. Sarkar, S. *et al.* Impaired autophagy in the lipid-storage disorder Niemann-Pick type C1 disease. *Cell Rep* **5**, 1302–1315, doi:10.1016/j.celrep.2013.10.042 (2013).
10. Oczypok, E. A., Oury, T. D. & Chu, C. T. It's a cell-eat-cell world: autophagy and phagocytosis. *Am J Pathol* **182**, 612–622, doi:10.1016/j.ajpath.2012.12.017 (2013).
11. Siegel, D. A. & Walkley, S. U. Growth of ectopic dendrites on cortical pyramidal neurons in neuronal storage diseases correlates with abnormal accumulation of GM2 ganglioside. *J Neurochem* **62**, 1852–1862 (1994).
12. Walkley, S. U., Siegel, D. A., Dobrenis, K. & Zervas, M. GM2 ganglioside as a regulator of pyramidal neuron dendritogenesis. *Ann N Y Acad Sci* **845**, 188–199 (1998).
13. Zervas, M., Dobrenis, K. & Walkley, S. U. Neurons in Niemann-Pick disease type C accumulate gangliosides as well as unesterified cholesterol and undergo dendritic and axonal alterations. *J Neuropathol Exp Neurol* **60**, 49–64 (2001).
14. Lawrence, R. E. & Zoncu, R. The lysosome as a cellular centre for signalling, metabolism and quality control. *Nat Cell Biol* **21**, 133–142, doi:10.1038/s41556-018-0244-7 (2019).
15. Howell, J. J. & Manning, B. D. mTOR couples cellular nutrient sensing to organismal metabolic homeostasis. *Trends Endocrinol Metab* **22**, 94–102, doi:10.1016/j.tem.2010.12.003 (2011).
16. Stiles, J. & Jernigan, T. L. The basics of brain development. *Neuropsychol Rev* **20**, 327–348, doi:10.1007/s11065-010-9148-4 (2010).
17. Ganesan, H. *et al.* mTOR signalling pathway - A root cause for idiopathic autism? *BMB Rep* **52**, 424–433 (2019).
18. Maue, R. A. *et al.* A novel mouse model of Niemann-Pick type C disease carrying a D1005G-Npc1 mutation comparable to commonly observed human mutations. *Hum Mol Genet* **21**, 730–750, doi:10.1093/hmg/ddr505 (2012).
19. Carracedo, A. & Pandolfi, P. P. The PTEN-PI3K pathway: of feedbacks and cross-talks. *Oncogene* **27**, 5527–5541, doi:10.1038/onc.2008.247 (2008).
20. Castellano, B. M. *et al.* Lysosomal cholesterol activates mTORC1 via an SLC38A9-Niemann-Pick C1 signaling complex. *Science* **355**, 1306–1311, doi:10.1126/science.aag1417 (2017).
21. Laplante, M. & Sabatini, D. M. Regulation of mTORC1 and its impact on gene expression at a glance. *J Cell Sci* **126**, 1713–1719, doi:10.1242/jcs.125773 (2013).
22. Camargo, N., Smit, A. B. & Verheijen, M. H. SREBPs: SREBP function in glia-neuron interactions. *FEBS J* **276**, 628–636, doi:10.1111/j.1742-4658.2008.06808.x (2009).

23. Wu, S. & Naar, A. M. SREBP1-dependent de novo fatty acid synthesis gene expression is elevated in malignant melanoma and represents a cellular survival trait. *Sci Rep* **9**, 10369, doi:10.1038/s41598-019-46594-x (2019).
24. Porstmann, T. *et al.* SREBP activity is regulated by mTORC1 and contributes to Akt-dependent cell growth. *Cell Metab* **8**, 224–236, doi:10.1016/j.cmet.2008.07.007 (2008).
25. Yi, J., Zhu, J., Wu, J., Thompson, C. B. & Jiang, X. Oncogenic activation of PI3K-AKT-mTOR signaling suppresses ferroptosis via SREBP-mediated lipogenesis. *Proc Natl Acad Sci U S A* **117**, 31189–31197, doi:10.1073/pnas.2017152117 (2020).
26. Pena-Llopis, S. & Brugarolas, J. TFEB, a novel mTORC1 effector implicated in lysosome biogenesis, endocytosis and autophagy. *Cell Cycle* **10**, 3987–3988, doi:10.4161/cc.10.23.18251 (2011).
27. Pena-Llopis, S. *et al.* Regulation of TFEB and V-ATPases by mTORC1. *EMBO J* **30**, 3242–3258, doi:10.1038/emboj.2011.257 (2011).
28. Napolitano, G. *et al.* mTOR-dependent phosphorylation controls TFEB nuclear export. *Nat Commun* **9**, 3312, doi:10.1038/s41467-018-05862-6 (2018).
29. Cupolillo, D. *et al.* Autistic-Like Traits and Cerebellar Dysfunction in Purkinje Cell PTEN Knock-Out Mice. *Neuropsychopharmacology* **41**, 1457–1466, doi:10.1038/npp.2015.339 (2016).
30. Busch, R. M. *et al.* Neurobehavioral phenotype of autism spectrum disorder associated with germline heterozygous mutations in PTEN. *Transl Psychiatry* **9**, 253, doi:10.1038/s41398-019-0588-1 (2019).
31. Kwon, C. H., Zhu, X., Zhang, J. & Baker, S. J. mTor is required for hypertrophy of Pten-deficient neuronal soma in vivo. *Proc Natl Acad Sci U S A* **100**, 12923–12928, doi:10.1073/pnas.2132711100 (2003).
32. Lim, C. Y. *et al.* ER-lysosome contacts enable cholesterol sensing by mTORC1 and drive aberrant growth signalling in Niemann-Pick type C. *Nat Cell Biol* **21**, 1206–1218, doi:10.1038/s41556-019-0391-5 (2019).
33. Shimano, H. & Sato, R. SREBP-regulated lipid metabolism: convergent physiology - divergent pathophysiology. *Nat Rev Endocrinol* **13**, 710–730, doi:10.1038/nrendo.2017.91 (2017).
34. Meltzer, S. *et al.* Phospholipid Homeostasis Regulates Dendrite Morphogenesis in Drosophila Sensory Neurons. *Cell Rep* **21**, 859–866, doi:10.1016/j.celrep.2017.09.089 (2017).
35. Ziegler, A. B. *et al.* Cell-Autonomous Control of Neuronal Dendrite Expansion via the Fatty Acid Synthesis Regulator SREBP. *Cell Rep* **21**, 3346–3353, doi:10.1016/j.celrep.2017.11.069 (2017).
36. Ang, M. J. *et al.* SREBP-1c Deficiency Affects Hippocampal Micromorphometry and Hippocampus-Dependent Memory Ability in Mice. *Int J Mol Sci* **22**, doi:10.3390/ijms22116103 (2021).
37. Kim, J., Kundu, M., Viollet, B. & Guan, K. L. AMPK and mTOR regulate autophagy through direct phosphorylation of Ulk1. *Nat Cell Biol* **13**, 132–141, doi:10.1038/ncb2152 (2011).
38. Kaneko, M. *et al.* Remodeling of monopolar Purkinje cell dendrites during cerebellar circuit formation. *PLoS One* **6**, e20108, doi:10.1371/journal.pone.0020108 (2011).

39. Palmieri, M. *et al.* mTORC1-independent TFEB activation via Akt inhibition promotes cellular clearance in neurodegenerative storage diseases. *Nat Commun* **8**, 14338, doi:10.1038/ncomms14338 (2017).
40. Palmieri, M., Pal, R. & Sardiello, M. AKT modulates the autophagy-lysosome pathway via TFEB. *Cell Cycle* **16**, 1237–1238, doi:10.1080/15384101.2017.1337968 (2017).
41. Martina, J. A., Chen, Y., Gucek, M. & Puertollano, R. MTORC1 functions as a transcriptional regulator of autophagy by preventing nuclear transport of TFEB. *Autophagy* **8**, 903–914, doi:10.4161/auto.19653 (2012).
42. Rocznik-Ferguson, A. *et al.* The transcription factor TFEB links mTORC1 signaling to transcriptional control of lysosome homeostasis. *Sci Signal* **5**, ra42, doi:10.1126/scisignal.2002790 (2012).
43. Cologna, S. M. A calcium message for Niemann-Pick type C. *J Cell Biol* **218**, 3890–3891, doi:10.1083/jcb.201911021 (2019).
44. Lloyd-Evans, E. *et al.* Niemann-Pick disease type C1 is a sphingosine storage disease that causes deregulation of lysosomal calcium. *Nat Med* **14**, 1247–1255, doi:10.1038/nm.1876 (2008).
45. Tiscione, S. A. *et al.* Disease-associated mutations in Niemann-Pick type C1 alter ER calcium signaling and neuronal plasticity. *J Cell Biol* **218**, 4141–4156, doi:10.1083/jcb.201903018 (2019).
46. Malek, M., Wawrzyniak, A. M., Ebner, M., Puchkov, D. & Haucke, V. Inositol triphosphate-triggered calcium release from the endoplasmic reticulum induces lysosome biogenesis via TFEB/TFE3. *J Biol Chem*, 101740, doi:10.1016/j.jbc.2022.101740 (2022).
47. Medina, D. L. *et al.* Lysosomal calcium signalling regulates autophagy through calcineurin and TFEB. *Nat Cell Biol* **17**, 288–299, doi:10.1038/ncb3114 (2015).
48. Tong, Y. & Song, F. Intracellular calcium signaling regulates autophagy via calcineurin-mediated TFEB dephosphorylation. *Autophagy* **11**, 1192–1195, doi:10.1080/15548627.2015.1054594 (2015).
49. Deus, C. M., Yambire, K. F., Oliveira, P. J. & Raimundo, N. Mitochondria-Lysosome Crosstalk: From Physiology to Neurodegeneration. *Trends Mol Med* **26**, 71–88, doi:10.1016/j.molmed.2019.10.009 (2020).
50. Yambire, K. F. *et al.* Mitochondrial biogenesis is transcriptionally repressed in lysosomal lipid storage diseases. *Elife* **8**, doi:10.7554/eLife.39598 (2019).
51. Goo, M. S. *et al.* Activity-dependent trafficking of lysosomes in dendrites and dendritic spines. *J Cell Biol* **216**, 2499–2513, doi:10.1083/jcb.201704068 (2017).
52. Roberts, V. J. & Gorenstein, C. Examination of the transient distribution of lysosomes in neurons of developing rat brains. *Dev Neurosci* **9**, 255–264, doi:10.1159/000111628 (1987).
53. Cardanho-Ramos, C. & Morais, V. A. Mitochondrial Biogenesis in Neurons: How and Where. *Int J Mol Sci* **22**, doi:10.3390/ijms222313059 (2021).
54. Li, G. *et al.* PTEN $\alpha$  regulates mitophagy and maintains mitochondrial quality control. *Autophagy* **14**, 1742–1760, doi:10.1080/15548627.2018.1489477 (2018).

55. Schafer, D. P. *et al.* Microglia sculpt postnatal neural circuits in an activity and complement-dependent manner. *Neuron* **74**, 691–705, doi:10.1016/j.neuron.2012.03.026 (2012).
56. Blanco, R. E., Vega-Melendez, G. S., De La Rosa-Reyes, V., Del Cueto, C. & Blagburn, J. M. Application of CNTF or FGF-2 increases the number of M2-like macrophages after optic nerve injury in adult *Rana pipiens*. *PLoS One* **14**, e0209733, doi:10.1371/journal.pone.0209733 (2019).

## Figures

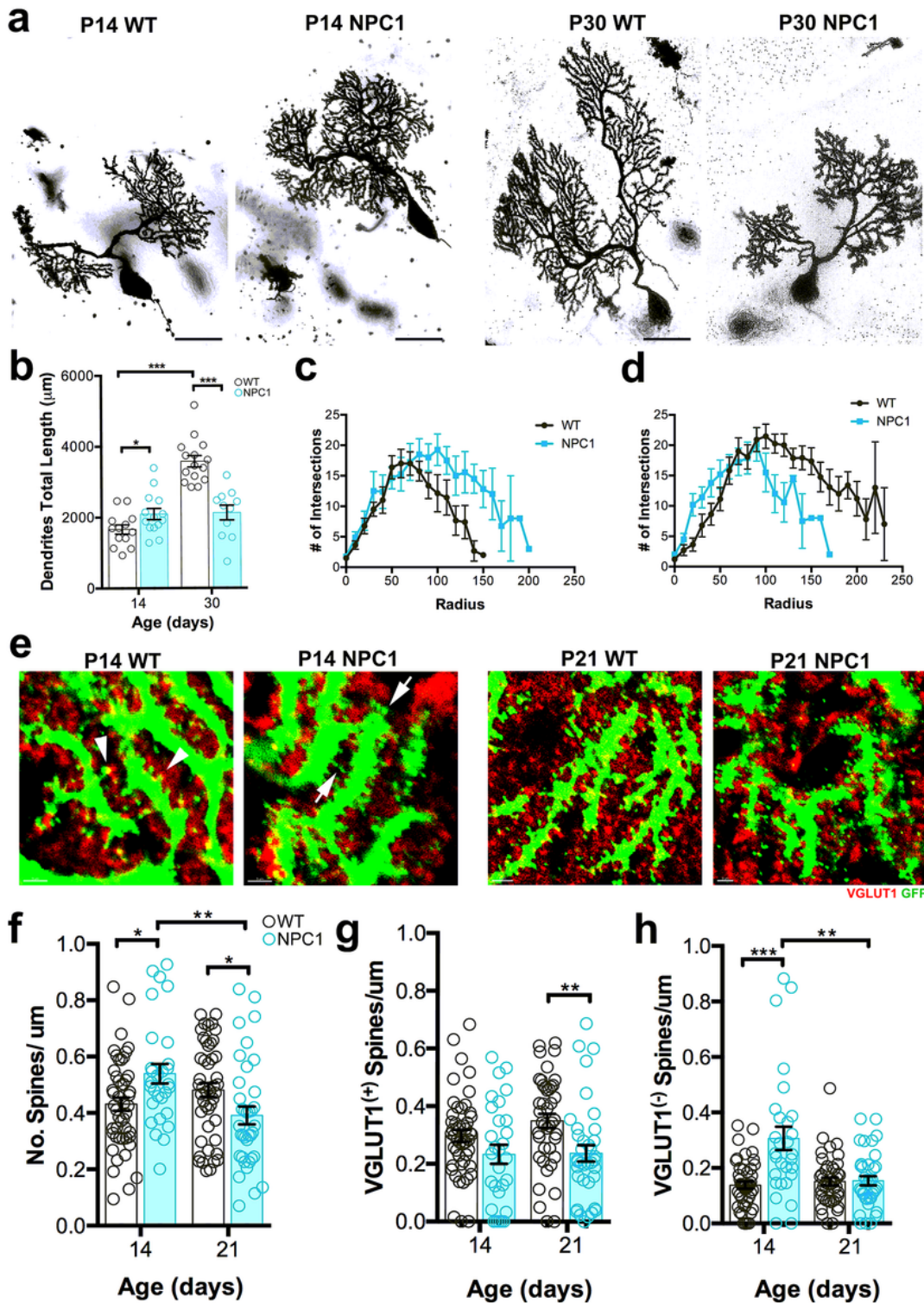
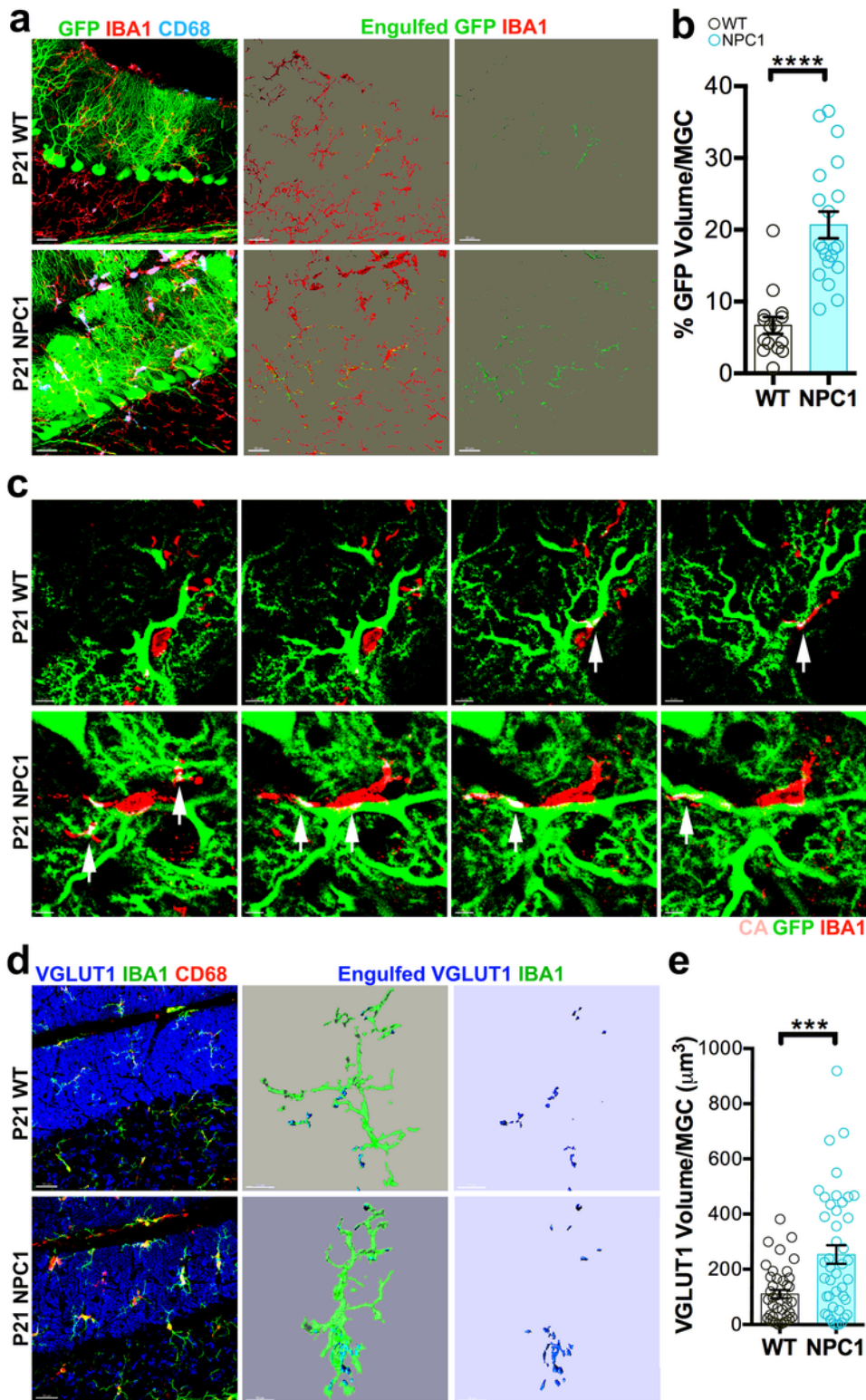


Figure 1

NPC1 deficiency alters the postnatal development of PC dendrites and synapses. **(a)** Golgi-Cox staining of PCs from WT and *Npc1<sup>nmf164</sup>* (NPC1) mice at P14 and P30. **(b)** Measurement of dendrites total length from PCs at P14 and P30 showing significant differences between WT and *Npc1<sup>nmf164</sup>* mice. Data are presented as mean  $\pm$  SEM,  $n=4$  mice/genotype/age, 4-5 cells/mouse. **(c)** Sholl-analysis showing differences in PC dendritic branching between WT and *Npc1<sup>nmf164</sup>* mice at P14. **(d)** Sholl-analysis

showing differences in PC dendritic branching between WT and *Npc1<sup>nmf164</sup>* mice at P30. **(e)** Interactions between GFP<sup>+</sup> PC dendritic spines and VGLUT1<sup>+</sup> presynaptic terminals in WT and *Npc1<sup>nmf164</sup>* mice at P14 and P21. Arrowheads showing VGLUT1<sup>(+)</sup> GFP<sup>+</sup> spines, arrows showing VGLUT1<sup>(-)</sup> GFP<sup>+</sup> spines. **(f)** Quantitative analysis of the total number of spines per mm. **(g)** Quantitative analysis of the number of spines that are contacted by VGLUT1<sup>+</sup> presynaptic terminals. **(h)** Quantitative analysis of the number of spines that are not contacted (VGLUT1<sup>(-)</sup>) by VGLUT1<sup>+</sup> presynaptic terminals. Data are presented as mean ± SEM, n=3-4 mice/genotype/age, n=10 dendritic segments/mouse. \*P < 0.05, \*\*P < 0.01, \*\*\*P < 0.001. Scale bar: (A) 20 mm (E) 3 mm.



**Figure 2**

Increased contacts and engulfment of PC dendritic GFP and VGLUT1<sup>+</sup> presynaptic inputs by microglia in P21 *Npc1<sup>nmf164</sup>* mice. **(a)** Confocal images and 3D surface renderings showing segregated IBA1<sup>+</sup> microglial cells from P21 WT and *Npc1<sup>nmf164</sup>* mice contacting or engulfing GFP<sup>+</sup> PC dendrites. The third column is showing 3D surface renderings of the contacted or engulfed GFP from PC dendrites. **(b)**

Quantitative analysis of the total volume of contacted or engulfed GFP<sup>+</sup> dendrites in P21 IBA1<sup>+</sup> microglia. **(c)** High magnified serial sections from the confocal Z stack in (a) showing GFP<sup>+</sup> dendrites contacted or engulfed (CA = contacted area, white arrows) by IBA1<sup>+</sup> microglia at P21. **(d)** Confocal images and 3D surface renderings showing segregated IBA1<sup>+</sup> microglial cells from P21 WT and *Npc1<sup>nmf164</sup>* mice contacting or engulfing VGLUT1<sup>+</sup> presynaptic inputs. The third column is showing 3D surface renderings of the contacted or engulfed VLUT1<sup>+</sup> presynaptic inputs. **(e)** Quantitative analysis of the total volume of contacted or engulfed VGLUT1<sup>+</sup> presynaptic inputs in P21 IBA1<sup>+</sup> microglia. Data are presented as mean  $\pm$  SEM, WT n=44 cells from 4 mice, *Npc1<sup>nmf164</sup>* n=46 cells from 4 mice. \*\*\*P < 0.001, \*\*\*\*P < 0.0001. Scale bars: (A) 30 mm, (C) 5mm, (D) 30mm.

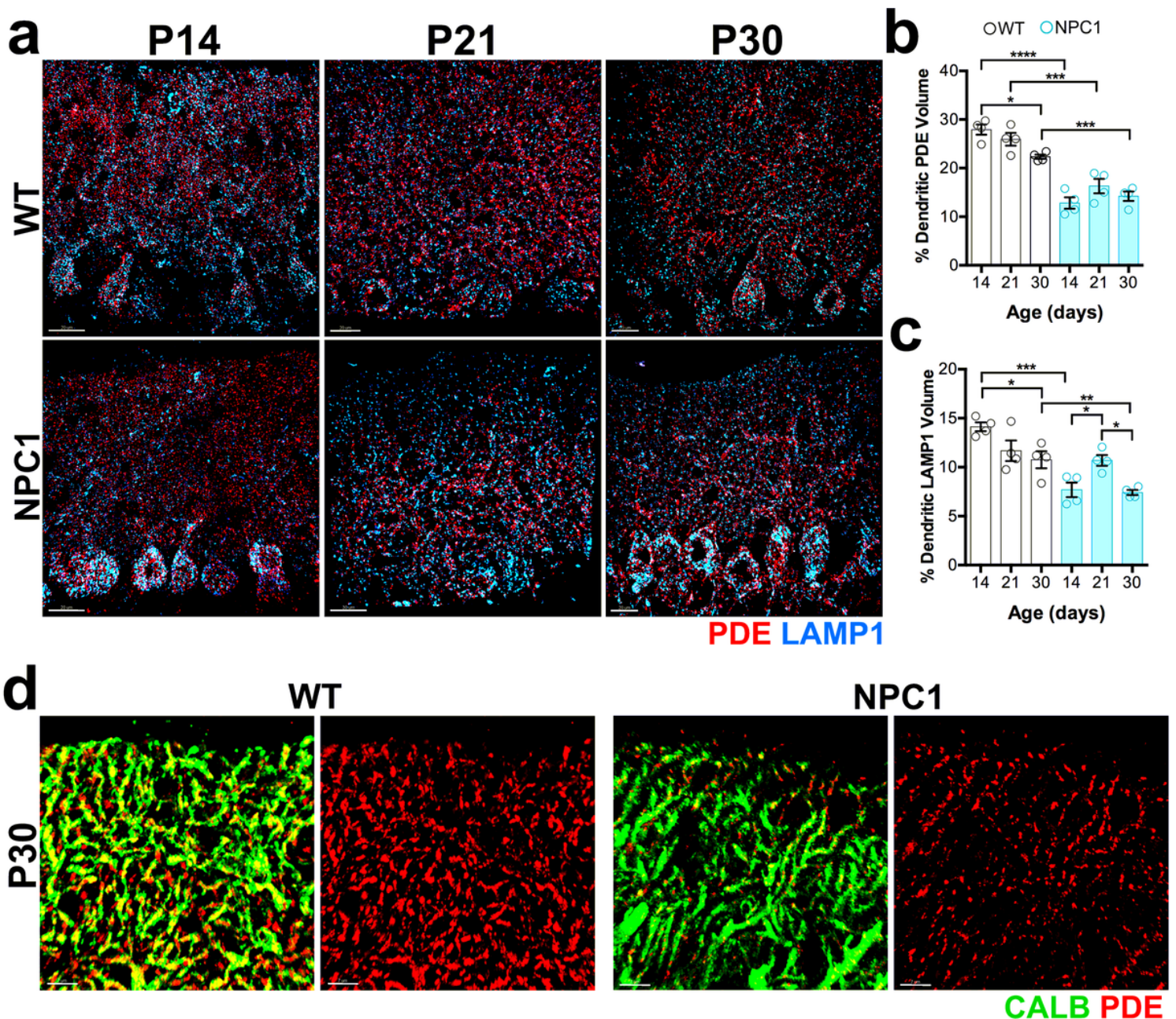


**Figure 3**

NPC1 deficiency decreases mitochondrial and lysosomal levels in PC dendrites during postnatal developmental stages. **(a)** Segregated PDE (mitochondria) and LAMP1 (lysosomes) immunostaining in PCs using Imaris software in WT and *Npc1<sup>nmf164</sup>* (NPC1) mice at P14, P21, and P30. **(b)** Measurement of the percentage of PDE volume in PCs dendrites at P14, P21, and P30 showing significant differences between WT and *Npc1<sup>nmf164</sup>* mice. **(c)** Measurement of the percentage of LAMP1 volume in PCs dendrites at P14, P21, and P30 showing significant differences between WT and *Npc1<sup>nmf164</sup>* mice. **(d)** Confocal images of PC dendrites immunostained with CALB and PDE showing the density, distribution, and morphology of dendritic mitochondria in PCs from P30 WT and *Npc1<sup>nmf164</sup>* mice. Data are presented as mean  $\pm$  SEM, n=4 mice/genotype. \*P < 0.05, \*\*P < 0.001, \*\*\*P < 0.001, \*\*\*\*P < 0.0001. Scale bar: (a) 20mm, (d) 7 mm,

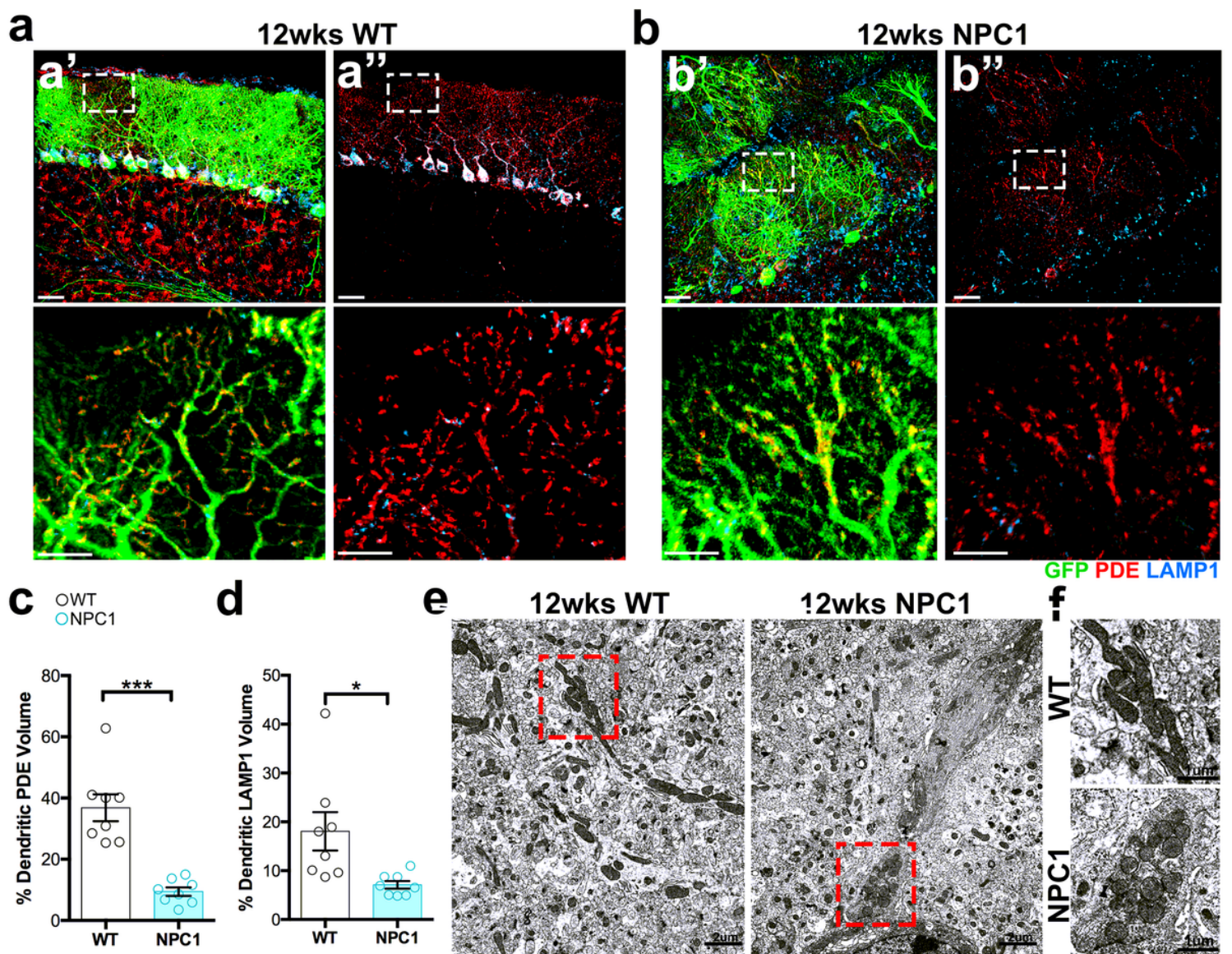


**Figure 4**

NPC1 deficiency decreases mitochondrial and lysosomal levels in 12wks PC dendrites during neurodegeneration. **(a-b)** Images of 12wks cerebellar sections showing the GFP<sup>+</sup> PCs in WT (a) and *Npc1<sup>nmf164</sup>* (b) mice immunolabeled with antibodies against PDE and LAMP (a' and b'). Fluorescent signal from PDE and LAMP1 only in PCs was segregated using the Imaris software for analysis (a'' and b''). High magnified images from insets in (a-b) show dendritic mitochondria density, distribution, and morphology. **(c)** Quantification of the percentage of PC dendritic PDE volume in WT and *Npc1<sup>nmf164</sup>* mice. **(d)** Quantification of the percentage of PC dendritic LAMP1 volume in WT and *Npc1<sup>nmf164</sup>* mice. Data are presented as mean  $\pm$  SEM, n=4 mice/genotype, 2 images/mouse. \*P < 0.05, \*\*P < 0.001, \*\*\*P < 0.001, \*\*\*\*P < 0.0001. **(e)** Transmission electron micrographs showing PCs dendrites segments containing mitochondria with significant differences in distribution and morphology between WT and *Npc1<sup>nmf164</sup>* mice. **(f)** Insets are magnified images from (e) showing mitochondria morphology and aggregation in *Npc1<sup>nmf164</sup>* mice. Scale bar: (a-b) 30  $\mu$ m and inset 10  $\mu$ m, (e) 2  $\mu$ m, (f) 1  $\mu$ m.

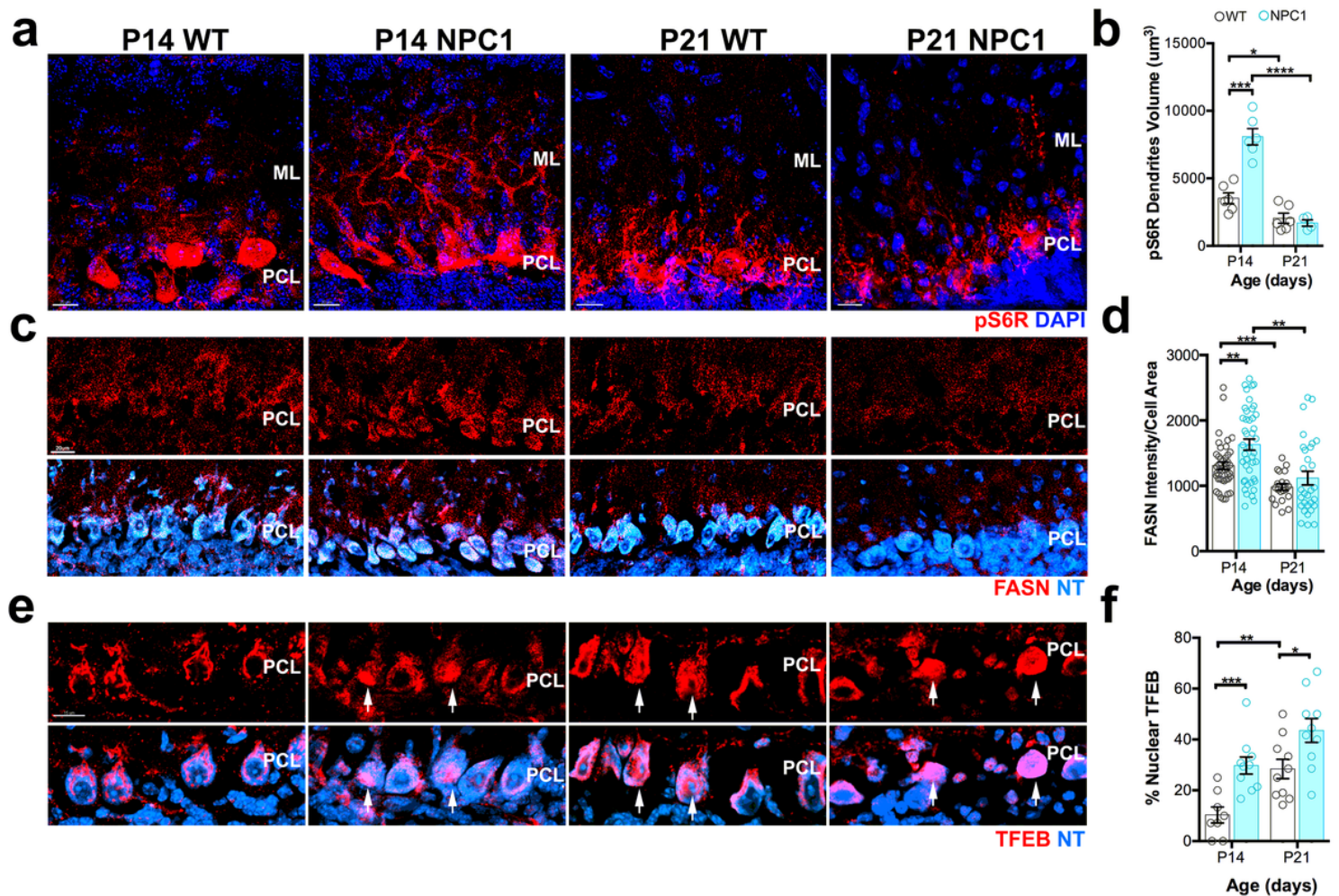


Figure 5

Simultaneous overactivation of the mTORC1 pathway and TFEB occurs in PCs from P14 *Npc1<sup>nmf164</sup>* mice. **(a)** Confocal images showing pS6R immunoreactivity in the cerebellar PCL and ML of P14 and P21 WT and *Npc1<sup>nmf164</sup>* mice. **(b)** Quantitative analysis of the total volume of pS6R in PC dendrites from WT and *Npc1<sup>nmf164</sup>* mice at P14 and P21. Data are presented as mean  $\pm$  SEM, n= 3 mice/genotype/age, 2 images/mouse. **(c)** Confocal images showing FASN immunoreactivity and NeuroTrace (NT) staining in the cerebellar PCL of P14 and P21 WT and *Npc1<sup>nmf164</sup>* mice. **(d)** Quantitative analysis of FASN fluorescence intensity in NT<sup>+</sup> PCs from WT and *Npc1<sup>nmf164</sup>* mice at P14 and P21. Data are presented as mean  $\pm$  SEM, n=10 cells/mouse from 4 mice/genotype/age. **(e)** TFEB immunoreactivity in PCs from WT and *Npc1<sup>nmf164</sup>* mice at P14 and P21; nuclear localization of TFEB is indicated by white arrows. **(f)** Percentage of PCs showing nuclear translocation of TFEB in WT and *Npc1<sup>nmf164</sup>* mice at P14 and P21. Data are presented as mean  $\pm$  SEM, n= 4 mice/genotype/age, 2-3 images/mouse. \*P < 0.05, \*\*P < 0.001, \*\*\*P < 0.001, \*\*\*\*P < 0.0001. Scale bars: (a) and (c) 20  $\mu$ m, (e) 15  $\mu$ m.

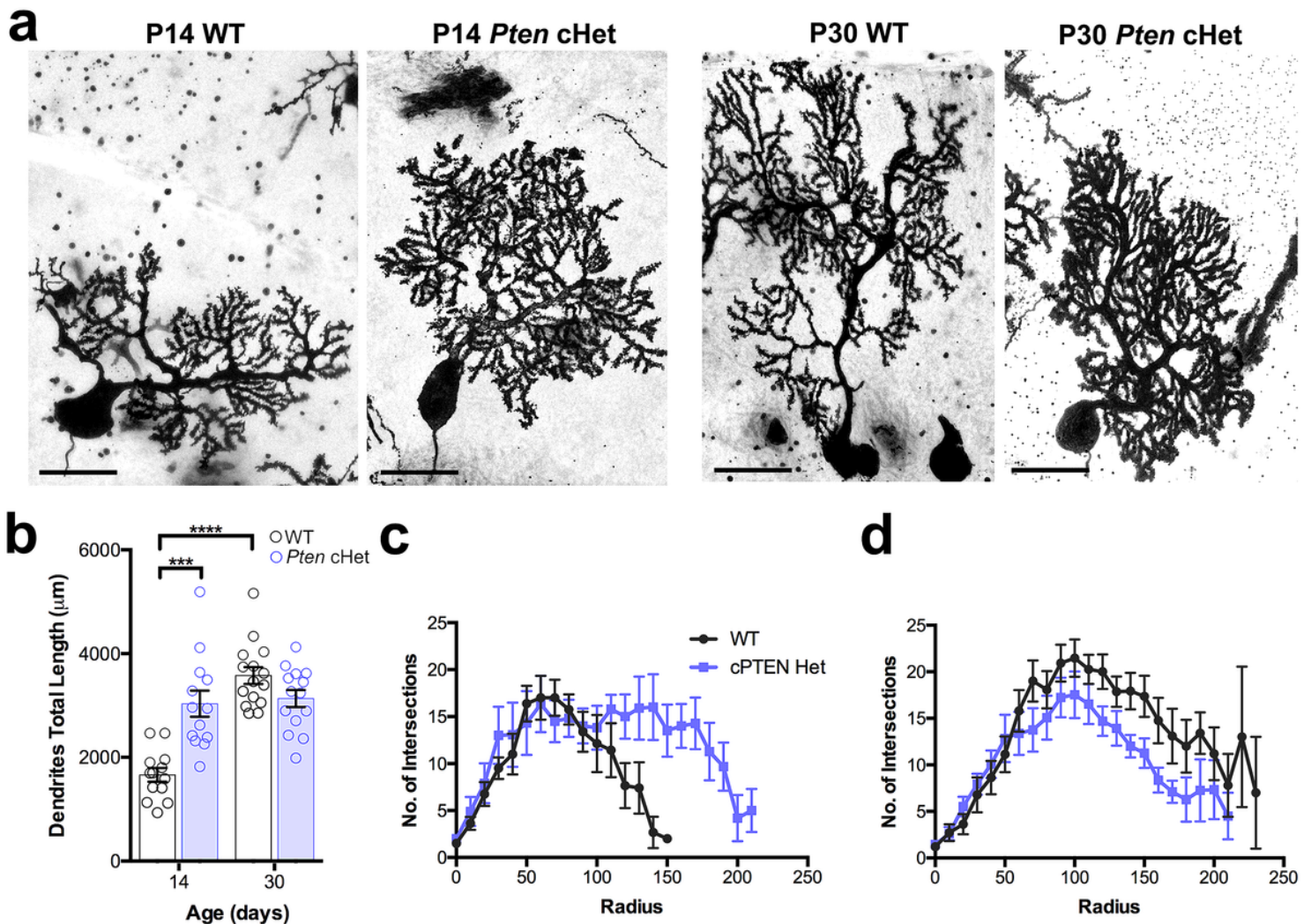
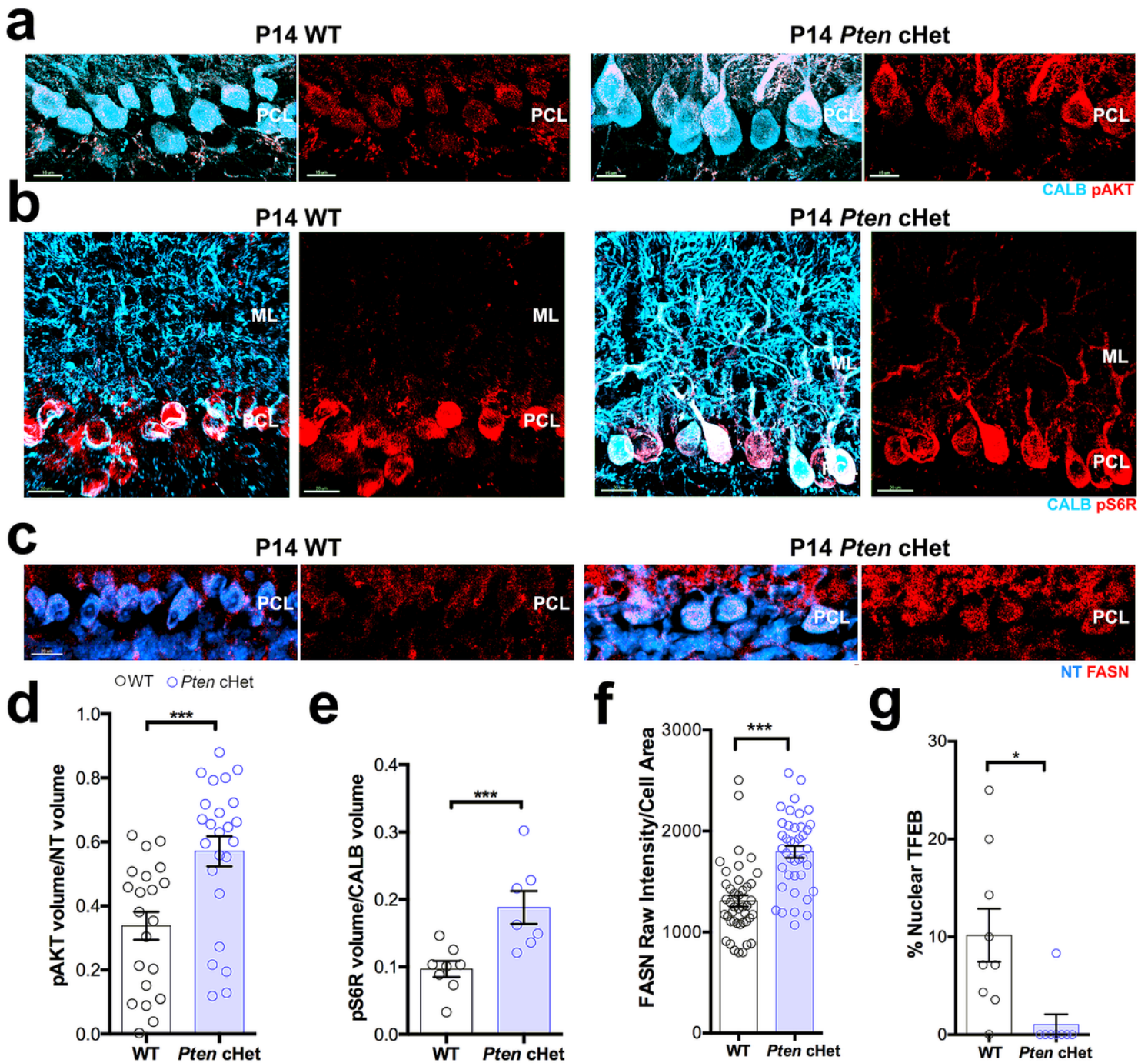


Figure 6

*Pten* conditional haploinsufficiency in PCs alters the postnatal development of their dendrites at P14. **(a)** Golgi-Cox staining of PCs from WT and *Pten*-cHet mice at P14 and P30. **(b)** Quantification of PC dendritic total length at P14 and P30 showing significant differences between WT and *Pten*-cHet mice at P14, no changes were found at P30. Data are presented as mean  $\pm$  SEM,  $n=4$  mice/genotype/age, 4-5 cells/mouse. **(c)** Sholl-analysis showing differences in PC dendritic branching between WT and *Pten*-cHet mice at P14. **(d)** Sholl-analysis showing differences in PC dendritic branching between WT and *Pten*-cHet mice at P30. Data are presented as mean  $\pm$  SEM,  $n=4$  mice/genotype/age, 4-5 cells/mouse. \*\*\* $P < 0.001$ , \*\*\*\* $P < 0.0001$ . Scale bar: (a) 20  $\mu$ m.



## Figure 7

Overactivation of the AKT-mTORC1 pathway in *Pten*-cHet PCs from P14 mice. **(a)** Confocal images showing pAKT and CALB immunoreactivity in P14 PCs from WT and *Pten*-cHet mice. **(b)** Confocal images showing pS6R and CALB immunoreactivity in the cerebellar PCL and ML of P14 WT and *Pten*-cHet mice. **(c)** Confocal images showing FASN immunoreactivity and NT staining in the cerebellar PCL of P14 WT and *Pten*-cHet mice. **(d)** Quantitative analysis of the ratio of pAKT volume in CALB<sup>+</sup> PC soma from WT and *Pten*-cHet mice at P14. Data are presented as mean  $\pm$  SEM, n= 4 mice/genotype/age, 5-6 cells/mouse. **(e)** Quantitative analysis of the ratio of pS6R volume per dendritic CALB volume from WT and *Pten*-cHet mice at P14. Data are presented as mean  $\pm$  SEM, n= 4 mice/genotype/age, 2 images/mouse. **(f)** Quantitative analysis of FASN fluorescence intensity in NT<sup>+</sup> PCs from WT and *Pten*-cHet mice at P14. Data are presented as mean  $\pm$  SEM, n=10 cells from 4 mice/genotype/age. **(g)** Quantitative analysis of the percentage of PCs with nuclear TFEB from WT and *Pten*-cHet mice at P14. Data are presented as mean  $\pm$  SEM, n= 2 images from 4 mice/genotype/age. \*\*\*P < 0.001. Scale bars: (a) 15  $\mu$ m, (b) and (c) 20  $\mu$ m.

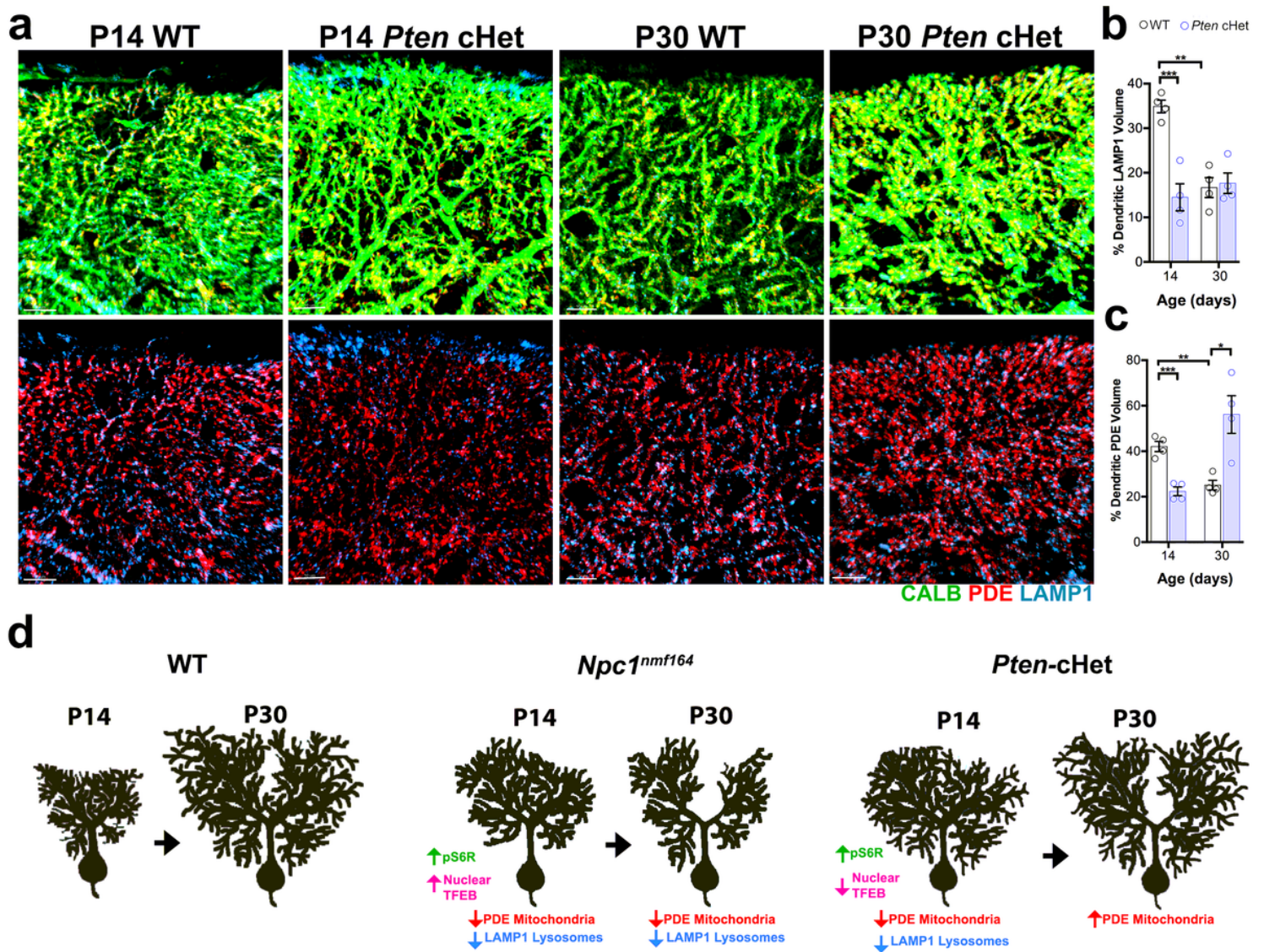


**Figure 8**

*Pten* conditional haploinsufficiency in PCs alters mitochondrial and lysosomal levels in PC dendrites during postnatal development. **(a)** Segregated PDE (mitochondria) and LAMP1 (lysosomes) immunostaining in CALB<sup>+</sup> PC dendrites in WT and *Pten*-cHet mice at P14 and P30. **(b)** Measurement of the percentage of LAMP1 volume in PCs dendrites at P14 and P30 showing significant differences between WT and *Pten*-cHet mice. **(c)** Measurement of the percentage of PDE volume in PCs dendrites at P14 and P30 showing significant differences between WT and *Pten*-cHet mice. Data are presented as mean ± SEM, n=4 mice/genotype/age. \*\*P < 0.001, \*\*\*P < 0.001. Scale bars: (A) 5 mm. **(d)** Schematic illustration showing how changes in activation of the mTORC1 pathway (pS6R) and TFEB occur along with significant changes in the size of the dendritic tree of PCs from *Npc1<sup>nmf164</sup>* and *Pten*-cHet mice during postnatal development. Changes in dendritic mitochondrial and lysosomal volume were evident in the different mouse strains, suggesting that lysosomal dysfunction in NPC1 deficient mice disturbs metabolic balance and causes dendritic atrophy.

## Supplementary Files

This is a list of supplementary files associated with this preprint. Click to download.

- [KimetalSupplementaryRevision.pdf](#)